

Modelling of tear propagation and arrest in fibre-reinforced soft tissue subject to internal pressure

Lei Wang · Steven M. Roper · X. Y. Luo ·
N. A. Hill

Received: 29 March 2014 / Accepted: 8 October 2014
© Springer Science+Business Media Dordrecht 2015

Abstract The prediction of soft-tissue failure may yield a better understanding of the pathogenesis of arterial dissection and help to advance diagnostic and therapeutic strategies for the treatment of this and other diseases and injuries involving the tearing of soft tissue, such as aortic dissection. In this paper, we present computational models of tear propagation in fibre-reinforced soft tissue undergoing finite deformation, modelled by a hyperelastic anisotropic constitutive law. We adopt the appropriate energy argument for anisotropic finite strain materials to determine whether a tear can propagate when subject to internal pressure loading. The energy release rate is evaluated with an efficient numerical scheme that makes use of adaptive tear lengths. As an illustration, we present the calculation of the energy release rate for a two-dimensional strip of tissue with a pre-existing tear of length a under internal pressure p and show the effect of fibre orientation. This calculation allows us to locate the potential bifurcation to tear propagation in the (a, p) plane. The numerical predictions are verified by analytical solutions for simpler cases. We have identified a scenario of tear arrest, which is observed clinically, when the surrounding connective tissues are accounted for. Finally, the limitations of the models and further directions for applications are discussed.

Keywords Arterial dissection · Energy release rate · Finite-element analysis · HGO model · Soft tissue · Tear propagation and arrest

1 Introduction

Failure of soft tissue can occur as a result of various diseases. In one particular disease, *aortic dissection*, a longitudinal tear occurs in the inner layer of the aortic wall, which results in the development of a false lumen that is formed as pressurised blood leaks into the tear. Aortic dissection is a life-threatening disorder; certain types of dissection, if left untreated, have a mortality rate of 33% within the first day, 50% within the first 2 days, and 75% within the first fortnight [1]. This pattern of mortality has remained essentially unchanged over the last 60 years [2], so early diagnosis and treatment is critical for survival. The advancement of diagnostic and therapeutic strategies depends crucially on improving our knowledge of the pathogenesis of aortic dissection.

L. Wang · S. M. Roper · X. Y. Luo (✉) · N. A. Hill
School of Mathematics and Statistics, University of Glasgow, Glasgow G12 8QW, UK
e-mail: Xiaoyu.Luo@glasgow.ac.uk

There are various hypotheses of the pathogenesis of aortic dissection, most of which involve three stages. Firstly, haemodynamic changes modify the loading on the arterial walls [3]; secondly, remodelling of the tissue occurs in response to the changed loading condition [4]; and thirdly, the mechanical environment changes owing to the presence of a small initial lesion. Of particular importance is the development of an understanding of the factors governing the propagation of the initial tear in the anisotropic soft tissue under blood pressure and large deformation. This is the focus of our paper.

Fibre-reinforced soft tissues are composed of a ground matrix and collagen fibres and are often characterised as being incompressible, hyperelastic, anisotropic and residually stressed. To model a tear in arteries, one may follow the approaches used to describe material failure in damage and fracture mechanics. Four of the commonly used mathematical theories are based on the stress intensity factor (SIF), the strain of individual components (the matrix and fibres), the cohesive zone and energy arguments.

The SIF criterion requires calculation of the stress field in the vicinity of the tip [5]. For a linear elastic isotropic material, the stress field near the tip is characterised by a stress intensity factor K which exhibits an $r^{-1/2}$ singularity, where r is the distance from the tip. A criterion for propagation is that, for a given mode of propagation, K is greater than a specified material toughness K_c ($K > K_c$). However, the asymptotic stress field near the tip is not generally known for finite-deformation non-linear elasticity, with the exception of simplified cases for isotropic power-law materials [6,7].

A failure criterion based on the representative strain of the individual components ϵ_i of soft tissue requires a model for considering the component strengths and modes of failure. Thus, the failure criterion can be expressed as $\epsilon_i > \epsilon_{ic}$, where ϵ_{ic} is the ultimate strain of the i th component just before failure. For example, Ionescu et al. [8] assume fibres fail when they are overstretched, but the matrix can be damaged under shear.

A cohesive zone approach was originally proposed for failure in concrete to model the process zone where the failure of the material takes place. A cohesive law gives equations relating normal and tangential displacement jumps across the cohesive surfaces at the front of a tip, to the tractions. It can be used to analyse tear propagation, nucleation, and arrest [9]. A cohesive law requires at least two parameters, the maximum tension just before failure and the work of dissipation, i.e. the area under the curve of cohesive traction against the relative displacement of the faces of the tear. Cohesive models have been used for the analysis of fracture in biological tissues for modelling a peeling test of an arterial strip under external loading [10]. Elices et al. [11] illustrated that the shape of a cohesive curve also has a significant effect on the simulation of failure, thus detailed experiments are required to determine the cohesive law for soft tissue [12]. Recently, Pandolfi and colleagues have developed anisotropic cohesive elements based on a standard finite-element method (FEM) for a strongly oriented fibre-reinforced material model [13–15] and used a direction-dependent resistance ellipsoid surface to reflect the anisotropic response of the material in the tearing process.

The energy approach to failure is based on calculating the *energy release rate* (ERR), G , which is the change in total potential energy, using per unit extension of the tear. It was developed by, among others, Griffith [16] and extended by Irwin and Wells [17]. Using the ERR to analyse the effects of defects historically preceded the use of the SIF and is equivalent to the cohesive zone model in some circumstances [18]. The concept of ERR stems from the energy balance principle during an infinitesimal quasi-static tear extension; it is the energy per unit area released from the system by extending the tear surface by an infinitesimal area dA . In plane strain, the deformation is two-dimensional and G is calculated per unit length instead of per unit area. Given the material parameter G_c , the critical energy required to break all bonds across dA , we can evaluate the potential for propagation of a tear: if $G > G_c$, then the tear may propagate (i.e. it is energetically feasible); otherwise, it is stationary. Thus, $G - G_c$ is the potential for tear propagation. In particular, ignoring any plastic effects, G can be calculated simply on the basis of the work done by loads and changes in strain energy accompanying the increase in tear area. Many numerical methods exist for calculating G , e.g. [19], and most rely, not on evaluating the singular stress field at the tip, but rather on the global energy and work, so an accurate value for G can be obtained with modest mesh refinement. Hence, for the arterial dissection problem, we choose to use the energy approach.

We use an invariant homogeneous fibre-reinforced material as a description for the aortic wall and focus on identifying the conditions that govern the onset of tear propagation. For simplicity, we assume that pressurised

blood fills the tear, and hence a false lumen is subject to the same arterial pressure as a true lumen, and we neglect flow in a small radial tear which connects the main dissection to the lumen. A finite-element model (FEM) is developed to study the finite elastic deformation of the aortic wall containing an initial tear and analyse the potential for tear propagation. We derive a failure criterion in terms of the ERR and describe a computational framework to calculate this. We illustrate the ideas by studying the behaviour of a tear in a two-dimensional strip of arterial material containing a single longitudinal tear. Using this computational framework, we obtain the condition for tear propagation in strips of material with different fibre distributions. In addition, we simulate the constraint arising from surrounding connective tissues and show that this can lead to tear arrest.

2 Methodology

2.1 Energy budget

A sample of tissue with a tear can deform and split apart when loaded, as illustrated in Fig. 1. The total potential energy of the system is

$$\mathcal{E} = \Pi + G_c a, \tag{1}$$

where the mechanical energy $\Pi = U_e - W$, U_e is the strain energy of the tissue sample at equilibrium, G_c is the energy required for breaking bonds linking the new torn surfaces (per unit area a in three dimensions, or per unit length a in two dimensions), and W is work done by the load. The minimal potential energy principle requires that

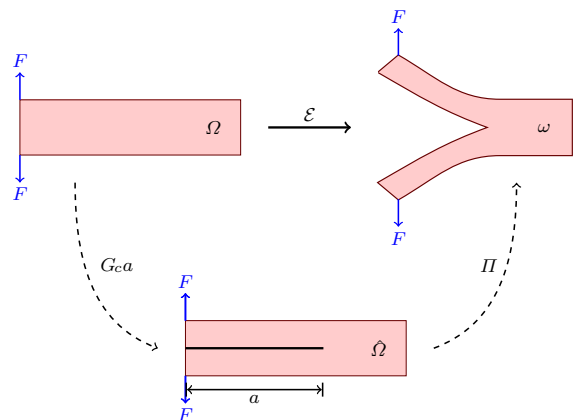
$$\frac{d\mathcal{E}}{da} < 0 \quad \text{or} \quad G > G_c, \tag{2}$$

where $G = -d\Pi/da$ is the ERR. To determine whether a tear may propagate, it is essential to first evaluate the ERR of the system.

2.2 Computational approach to calculating ERR

A simplified geometry for the arterial tissue is employed. A key clinical observation is that many patients present with a dissection of fixed length at risk of further tearing. We seek to determine the conditions under which a tear of finite length will propagate in a large artery via the criterion given in (2). The geometry is simplified by modelling the artery as a cylinder with an axisymmetric tear subject to constant pressure p , approximating the blood pressure

Fig. 1 A change in the sample under force F , $\Omega \rightarrow \omega$, can be approached in two steps: creating a tear of area a , $\Omega \rightarrow \hat{\Omega}$, followed by elastic deformation, $\hat{\Omega} \rightarrow \omega$. Correspondingly, the total potential energy for the system, \mathcal{E} , is decomposed into surface energy, $G_c a$, and mechanical energy, Π



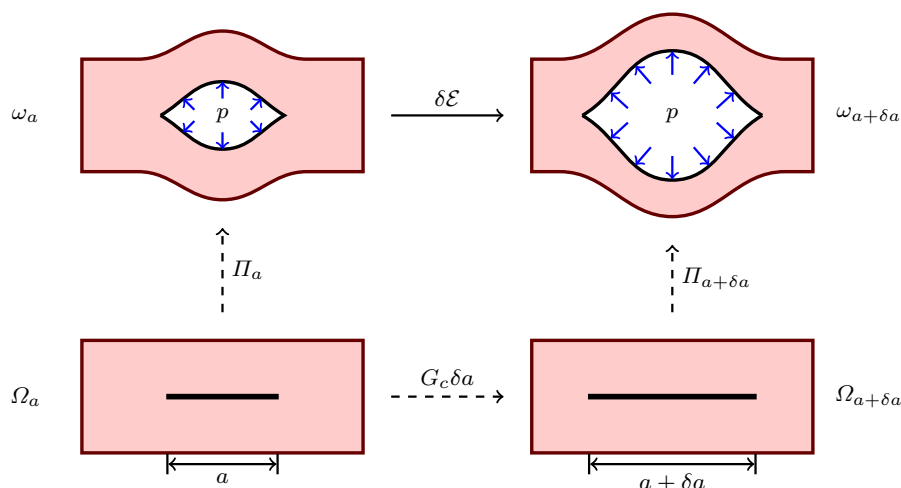


Fig. 2 The variation in total potential energy due to a tear propagation from ω_a to $\omega_{a+\delta a}$ is $\delta\mathcal{E} = \delta\Pi + G_c\delta a = (\Pi_{a+\delta a} - \Pi_a) + G_c\delta a$. To obtain Π for the calculation of the ERR in (3), we calculate the equilibria of Ω_a and $\Omega_{a+\delta a}$ subject to a constant uniform pressure, p , on the tear surfaces using the FEM

by its mean value, neglecting the small communicating tear between the lumen and main dissection, considering a cross-section through the wall and simplifying further to a two-dimensional strip, ω_a (Fig. 2).

For hyperelastic anisotropic soft tissues undergoing finite deformation, criterion (2) must be evaluated numerically. There are two methods for calculating the ERR using the FEM. One is based on the variation in local energy in the vicinity of the tip; the other is based on the variation in the global energy [20]. We adopt the latter approach because it allows us to avoid any difficulties when it is extended to finite-deformation non-linear elasticity, even when body forces and residual stresses are included. The formula for calculating a numerical approximation to G is

$$G = -\frac{\delta\Pi}{\delta a} = -\frac{\Pi_{a+\delta a} - \Pi_a}{\delta a}. \quad (3)$$

To obtain the equilibrium value of Π_a , we solve a specified boundary value problem using the FEM package FEAP [21]. With pressure loading, the solution can be obtained by a *proportional load process*, in which the loading parameter is increased (parametrised by an artificial ‘time’ t) incrementally towards its final value and the solution is updated at each increment. Depending on the material parameters and the particular method used to solve the discretised equations, this calculation can be time consuming. To improve computational efficiency, we incorporate interpolation techniques for Π_a . We evaluate Π_a for a collection of lengths and use cubic spline interpolation between these values. This gives a smooth approximation to $\Pi(a)$ which can be used to estimate $G = -d\Pi/da$. The numerical procedure relies on the numerical calculations of the strain energy U_e and the work done by external load W , which we now describe.

2.3 Calculation of strain energy U_e

For arterial tissue, we use the Holzapfel–Gasser–Ogden (HGO) constitutive law [22], which is based on the histology of the artery. The strain energy function in the HGO model is split into contributions from the matrix Ψ_m and the fibres Ψ_f , viz.

$$\bar{\Psi}(\mathbf{C}) = \Psi_m(I_1) + \Psi_f(I_4, I_6) = \frac{c}{2}(I_1 - 3) + \sum_{n=4,6} \psi(I_n), \quad (4)$$

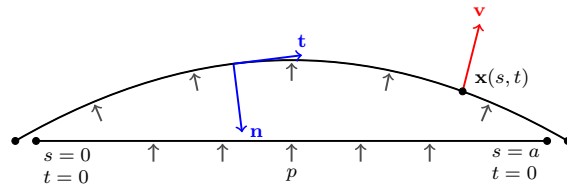


Fig. 3 Sketch of deformation of one tear surface under constant pressure: \mathbf{t} and \mathbf{n} are the tangent and normal unit vectors of the deformed tear surface, respectively, and \mathbf{v} is the velocity of the particle at time t which originated at $\mathbf{x} = \mathbf{x}(s, 0)$

where the two fibre families, aligned along the reference unit vector directions \mathbf{A}_1 and \mathbf{A}_2 , only contribute when stretched and are given by

$$\psi(I_n) = \begin{cases} \frac{k_1}{2k_2} [\exp(k_2(I_n - 1)^2) - 1] & \text{when } I_n > 1, \\ 0 & \text{when } I_n \leq 1. \end{cases} \tag{5}$$

In (4) and (5), c , k_1 , and k_2 are material parameters, and I_1 and I_n ($n = 4, 6$) are invariants of the right Cauchy–Green strain tensor $\mathbf{C} = \mathbf{F}^T \mathbf{F}$, specifically

$$I_1 = \text{tr}(\mathbf{C}), \quad I_n = \mathbf{C} : \mathbf{M}_n \quad (n = 4, 6),$$

with \mathbf{F} being the deformation gradient, $\mathbf{M}_4 = \mathbf{A}_1 \otimes \mathbf{A}_1$, and $\mathbf{M}_6 = \mathbf{A}_2 \otimes \mathbf{A}_2$.

To approximate the incompressible behaviour in the finite-element calculation, we employ the multiplicative decomposition of the deformation gradient [23] to form a quasi-incompressible material model

$$\Psi(\mathbf{C}) = \Psi_v(J) + \bar{\Psi}(\bar{\mathbf{C}}) = \frac{K}{2}(J - 1)^2 + \bar{\Psi}(\bar{\mathbf{C}}), \tag{6}$$

where $J = \det(\mathbf{F})$ and $\bar{\mathbf{C}} = J^{-2/3} \mathbf{C}$. The incompressibility condition is satisfied to a good approximation when the penalty constant K is large enough. The Cauchy stress is then

$$\boldsymbol{\sigma} = -\frac{d\Psi_v}{dJ} \mathbf{1} + c \text{dev}(\mathbf{b}) + \sum_{n=4,6} 2 \frac{d\psi}{dI_n} \text{dev}(\mathbf{m}_n), \tag{7}$$

where $\mathbf{b} = \mathbf{F} \mathbf{F}^T$, $\mathbf{m}_n = \mathbf{F} \mathbf{M}_n \mathbf{F}^T$ and $\text{dev}(\cdot) = (\cdot) - \frac{1}{3} \text{tr}(\cdot) \mathbf{1}$. A detailed derivation of the HGO model for a user subroutine in FEAP [24] is shown in Appendix 1. The verification of the model is discussed in Appendix 2.

2.4 Calculation of work done by pressure

Consider the tear surface specified by a position vector $\mathbf{x} = \mathbf{x}(s, t)$, $0 \leq s \leq a$, $0 \leq t \leq T$, as shown in Fig. 3. At time $t = 0$, $\mathbf{x}(s, 0)$ specifies the initial tear surface. The force on a small portion of the tear of length dl is

$$d\mathbf{f} = -p \, dl \, \mathbf{n} = -p \left| \frac{\partial \mathbf{x}}{\partial s} ds \right| \mathbf{n},$$

and the work done in a small time dt is

$$dw = d\mathbf{f} \cdot \mathbf{v} \, dt = d\mathbf{f} \cdot \frac{\partial \mathbf{x}}{\partial t} dt.$$

The work done by the distributed force (pressure) is then

$$W = \int dw = -p \int_0^T \int_0^a \mathbf{n} \cdot \frac{\partial \mathbf{x}}{\partial t} \left| \frac{\partial \mathbf{x}}{\partial s} \right| ds \, dt. \tag{8}$$

Table 1 Characterisation of materials used in four numerical experiments on effect of fibres

Experiment	Material type	\mathbf{A}_1	\mathbf{A}_2
1	Isotropic	N/A	N/A
2	Transversely isotropic	(1, 0, 0)	(1, 0, 0)
3	Orthotropic	($\cos(\pi/4)$, $\sin(\pi/4)$, 0)	($\cos(\pi/4)$, $-\sin(\pi/4)$, 0)
4	Transversely isotropic	(0, 1, 0)	(0, 1, 0)

Let \mathbf{k} be the unit vector along the third direction into the diagram; then $\mathbf{n} = \mathbf{k} \times \mathbf{t}$ and $\mathbf{t} = \frac{\partial \mathbf{x}}{\partial s} \left| \frac{\partial \mathbf{x}}{\partial s} \right|^{-1}$. Substituting these expression into (8) gives

$$W = -p \int_0^T \int_0^a \left(\mathbf{k} \times \frac{\partial \mathbf{x}}{\partial s} \right) \cdot \frac{\partial \mathbf{x}}{\partial t} ds dt. \quad (9)$$

The triple product is the signed volume of the parallelepiped defined by the three vectors and $|\mathbf{k}| = 1$; therefore, the integral in (9) represents the area swept by the tear surface.

3 Results

3.1 Numerical experiments

Consider a strip with two ends fixed in the y -axis direction, as shown in Fig. 4. To avoid rigid body motions, the x -coordinate of the centreline of the strip is fixed. For a tear under the pressure loading, we consider the ERR due to the tear extension for four different materials, one without fibres and the others with different fibre orientations (Table 1). In all cases, we set the values of the material parameters in the constitutive law (5) at $c = 3.0$ kPa, $k_1 = 2.3632$ kPa and $k_2 = 0.8393$, which are typical values for the media of rabbit carotid artery [22].

3.1.1 Isotropic material

We seek a condition for the onset of tear propagation as a function of tear length and pressure, and so we calculate $G(a, p)$. In particular, we consider the possibility of propagation for a tear of length $a \in [0.4, 10.0]$ mm subject to pressure $p \in [0, 0.6]$ kPa.

In the numerical Experiment 1, the strip has no fibres and is isotropic. The ERR $G(a, p)$ is a monotonically increasing function of a for each value of p , as shown in Fig. 5. A longer tear leads to an increased ERR and, thus, an increase in the likelihood of tear propagation. This observation agrees with the results of a beam model described in Appendix 3 [see Eq. (26)]. A comparison of the curves for different pressures shows that $G(a, p)$ is also a monotonically increasing function of p for fixed values of a , in agreement with high pressure favouring tear propagation.

3.1.2 Fibre-reinforced materials

To investigate the effect of collagen fibres on the ERR, we perform three more numerical experiments by reinforcing the strip with fibres of different orientations. In Experiment 2, the fibres are parallel to the tear, in Experiment 3 the fibres are aligned at $\pi/4$ to the tear, and in Experiment 4 the fibres are normal to the tear, as specified by the alignment vectors \mathbf{A}_1 and \mathbf{A}_2 in Table 1.

The curves of $G(a)$ when $p = 0.6$ kPa are shown in Fig. 6. The curve for Experiment 2 is very close to that for Experiment 1. The fibres can only support loads in tension, and the regions with subject to stretch are small and only occur just ahead of the tear tips (Fig. 7). Consequently, the tear opening and stored energy, and thus the mechanical energy, are similar to those for Experiment 1 (Fig. 8).

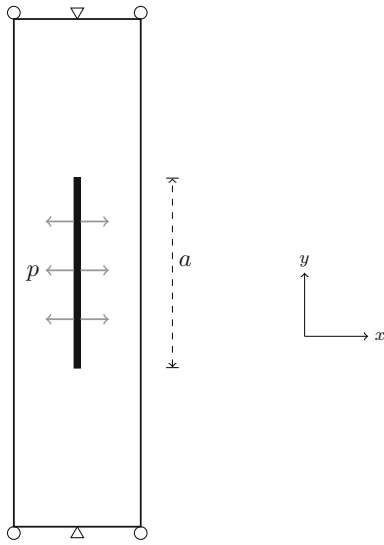


Fig. 4 Sketch of strip with single longitudinal tear of length a under internal pressure p . Boundary conditions: the two ends are fixed in the y -direction, and the centres of the two ends are fixed in the x -direction

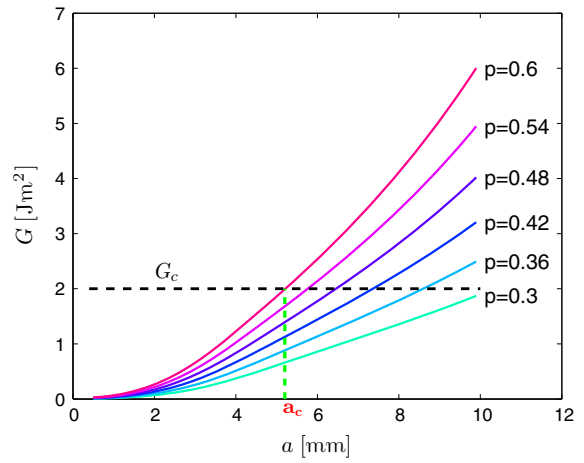


Fig. 5 Energy release rate G for a fibre-free isotropic strip, plotted against tear length a subject to various values of pressure p . G_c is a material-dependent critical parameter, and when, for example, $G_c = 2 \text{ Jm}^{-2}$ and $p = 0.6 \text{ kPa}$, it is energetically favourable for a tear of length greater than a_c to propagate

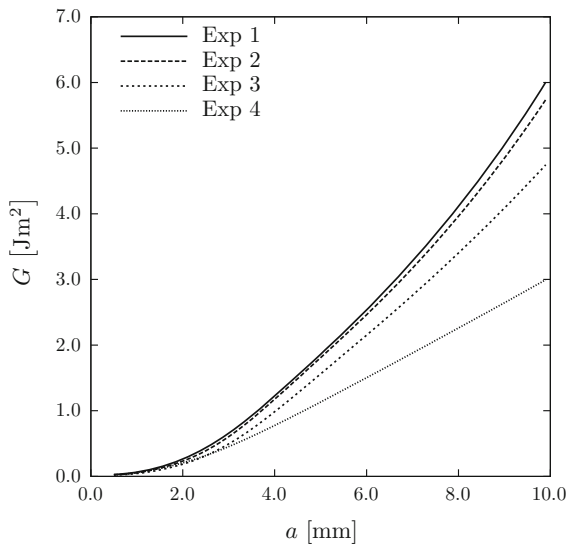


Fig. 6 Graphs of ERR $G(a)$ when $p = 0.6 \text{ kPa}$ for four numerical experiments listed in Table 1. G decreases as the angle between the fibres and the tear decreases

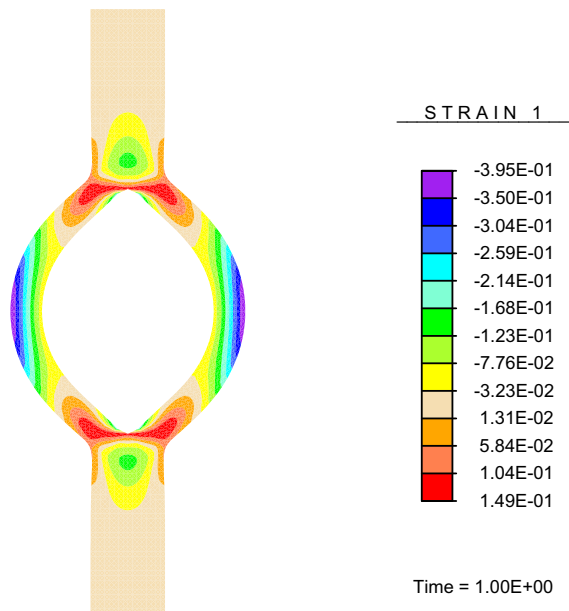


Fig. 7 First component of Almansi strain tensor $e_{11} = \frac{1}{2}(1 - I_4^{-1})$ for Experiment 2. The regions with positive values, close to the tear tips, indicate fibre stretching

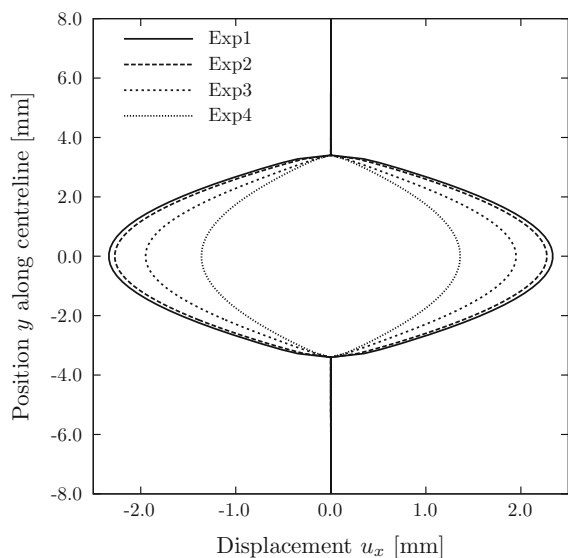


Fig. 8 Width of tear with pressure $p = 0.6$ kPa for four numerical experiments listed in Table 1. As the fibres become more parallel to tear, the width of tear decreases

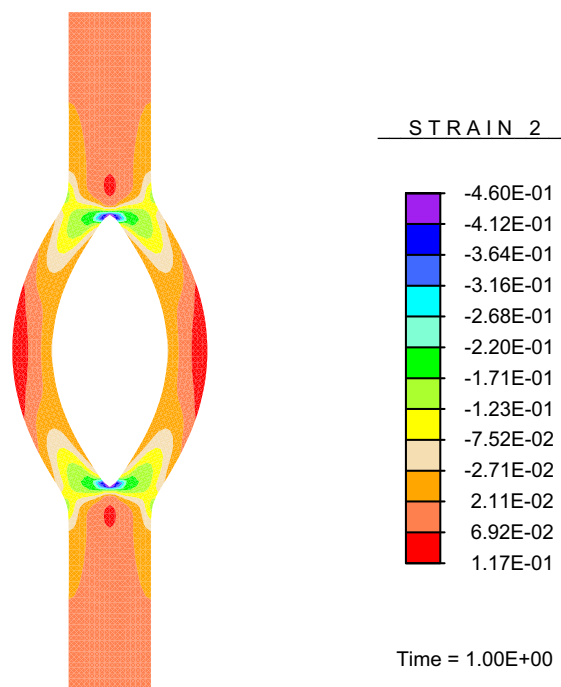


Fig. 9 Second component of Almansi strain tensor $e_{22} = \frac{1}{2}(1 - I_4^{-1})$ for Experiment 4. The positive values indicate fibre stretching

As the fibres become more parallel to the tear going from Experiment 2 to Experiment 4, the ERR decreases because the fibres take on a greater load to resist the opening of the tear, as shown in Fig. 8. Specifically, the region with stretch along the fibre direction in Experiment 4 (Fig. 9) is greater than that in Experiment 2 (Fig. 7). $G(a, p)$ is also shown as a contour plot in Fig. 10. The region at highest risk of tear propagation is at the top right-hand corner. These contours are similar in all four numerical experiments.

3.2 Effects of connective tissue: tear arrest

To consider the effect on tear propagation of the connective tissue around the strip, we add two linearly elastic blocks to the sides of the strip in the computational model. The reference configuration and boundary conditions are shown in Fig. 11. The central strip is the fibre-free material used in Experiment 1. The ERR plots in Fig. 12 show that arrest of the tear propagation can occur due to the surrounding connective tissue resisting the deformation of the strip. Arrest of the propagation of the tear is also found in the simple beam model described in Appendix 3 (Fig. 17). However, for softer connective tissue (with a Young's modulus of $E = 0.01$ kPa instead of $E = 10$ kPa), the arrest phenomenon disappears (Fig. 13), and so the stiffness of the surrounding connective tissue is an essential factor influencing the likelihood of tear propagation.

4 Discussion

In this paper, we have developed models to evaluate the likelihood of tear propagation in soft tissue with the failure criterion expressed in terms of the ERR. Models which build on the energy balance apply equally well to both

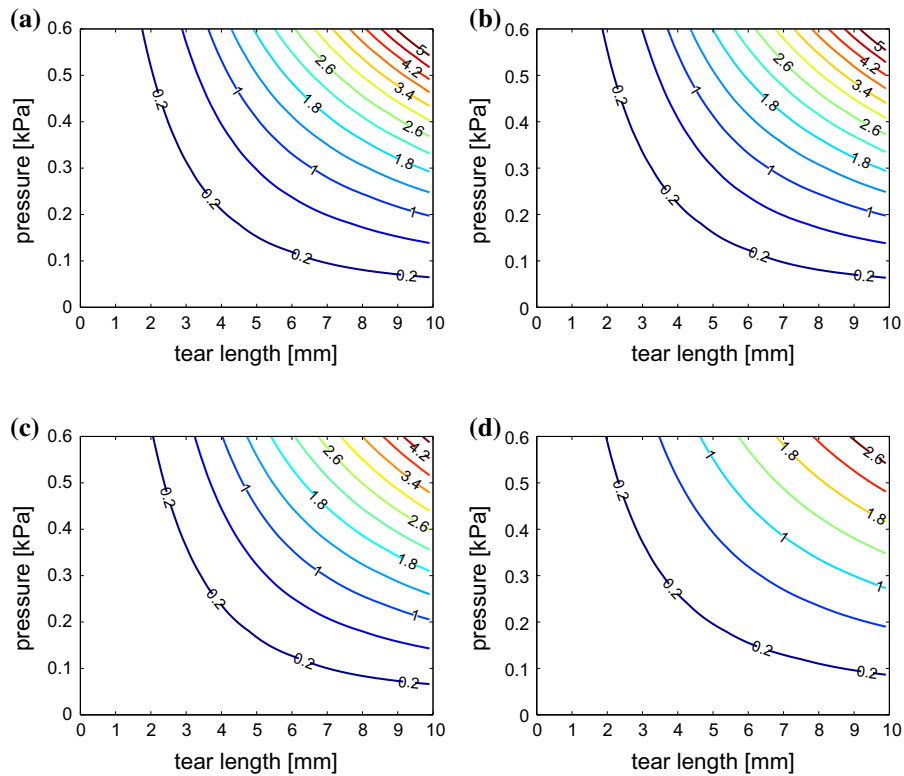


Fig. 10 Contours of $G(a, p)$ for four numerical experiments in Table 1. The region at highest risk of tear propagation lies at the top right-hand corner **a** Exp.1, **b** Exp. 2, **c** Exp. 3, **d** Exp. 4

linearly elastic isotropic problems and to finite strain and anisotropic problems, and provide useful theoretical insight in the absence of detailed experimental data. By assuming tear propagation to be an isothermal process, we explored whether a pre-existing dissection could propagate in artery walls subject to constant pressure. Such an approach can be used to evaluate the risk of propagation of aortic dissection and other injuries to soft tissue.

A key element of the energy approach is to evaluate the change in the energy budget with the tear size, which is non-trivial for finite strain and fibre-reinforced soft tissue problems. Using a nearly incompressible HGO orthotropic constitutive law, in conjunction with a penalty method, we have developed an efficient computational model which allows us to calculate the ERR for incompressible soft tissues. In particular, the ERR due to the tear extension is estimated by incorporating an interpolation technique on $\Pi(a)$ for the sake of computational efficiency.

Qualitative verification of the computational models was carried out. This included testing the models for simple cases where analytical solutions are available. In addition, we found that the ERR from the computational models had qualitatively the same trend as the ERR predictions from a beam model (Appendix 3) for the isotropic material.

Although the exact failure threshold depends on the tissue properties, the energy behaviour of such materials owing to a pre-existing tear is clearly demonstrated through the contours of the ERR in the tear-length and pressure space, (a, p) . For both isotropic and fibre-reinforced materials with different fibre orientations, we use numerical experiments to show that the risk of tear propagation increases with both a and p . Interestingly, the particular fibre structure changes the gradient of the ERR curve, with non-fibrous (isotropic) material producing the steepest increase (Experiment 1), followed by cases where the alignment of the fibres is normal (Experiment 2) and oblique (Experiment 3) to the tear. In the case where the fibres are aligned parallel to the tear, the gradient is least steep (Experiment 4). This shows that the presence of fibres reduces the risk of tear propagation and that the orientation of the fibres also plays an important role. This effect may be more pronounced in physiological scenarios since the fibre–matrix interaction is represented simply in our models.

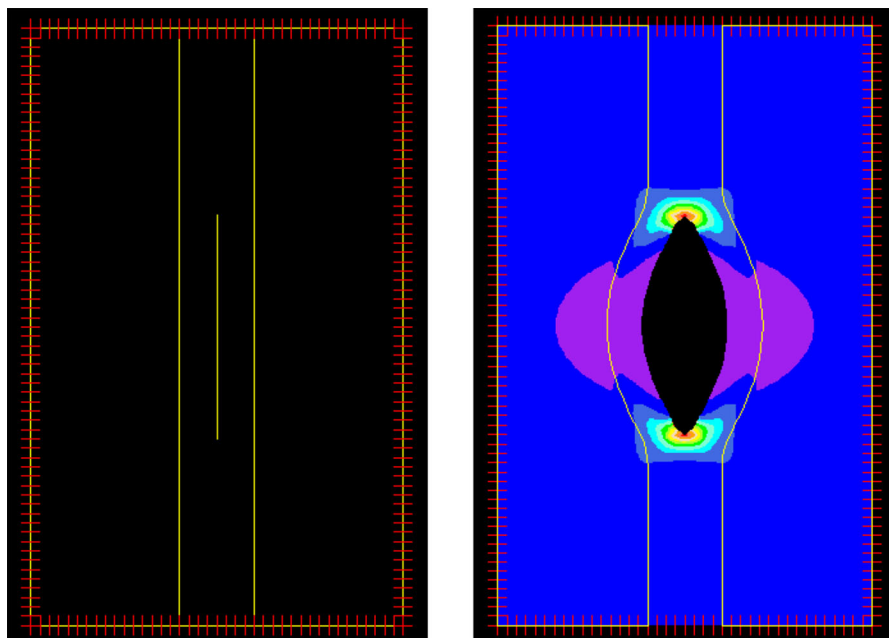


Fig. 11 Reference configuration and current configuration of strip when constrained by two blocks. The tear surfaces are loaded with constant pressure. The outer boundaries of the confining blocks are constrained so that they cannot move in the direction perpendicular to the axis of the tear. The ends of the strip and block are constrained so they cannot move in the direction parallel to the direction of the tear

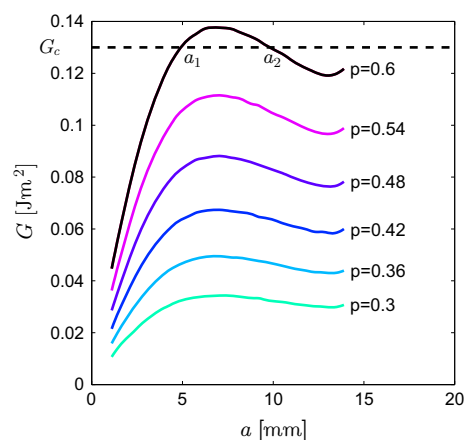


Fig. 12 Graphs of ERR G for a strip constrained by two linearly elastic blocks, as shown in Fig. 11. For example, when $G_c = 0.13 \text{ Jm}^{-2}$ and $p = 0.6 \text{ kPa}$, it is only energetically favourable for a tear to propagate when its length $a \in (a_1, a_2)$ (cf. Fig. 5)

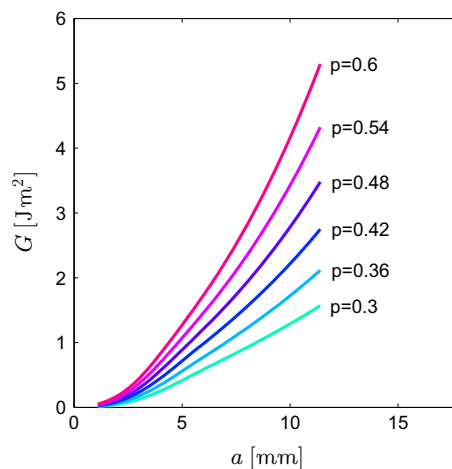


Fig. 13 In contrast to Fig. 12, where the Young's modulus of the surrounding tissue is $E = 10 \text{ kPa}$, the ERR $G(a)$ in the case with much softer surrounding tissue ($E = 0.01 \text{ kPa}$) is always a monotonically increasing function of the tear length, a , and tear arrest cannot occur

Our study shows that for a given pressure, the ERR increases monotonically with tear length. In other words, once a tear is initiated, it will always grow. However, when the effects of connective tissues are considered, both computational and beam models predict tear arrest. That is, at some critical values of a , the ERR decreases with an increase in a . Tear arrest is observed clinically since patients with aortic dissection which has arrested are then at the risk of further propagation of the dissection. This is the first time that tear arrest in soft tissues has been demonstrated

in computational models. We also found that tear arrest only occurs when the Young’s modulus of the surrounding connective tissue is sufficiently great, suggesting that disease-induced softening of connective tissues may lead to further tear propagation. Although our study is only qualitative and is not based on physiological geometries, this finding nevertheless enhances our understanding of the relationship between pathological conditions of connective tissues and arterial dissection.

Finally, we would like to mention the limitations of the study. To establish basic concepts without going into complex numerical modelling, we consider two-dimensional homogeneous tissue strips in which the tear can only propagate along its original direction since the geometry, material and load are symmetric. A natural next step would be to extend our approach to three-dimensional thick-walled tube models and include the effects of residual stress or opening angles, which will change the stress and ERR distributions. Another limitation of this study is that we have specified the tear propagation direction based on the symmetry in our chosen examples. When the method is extended to three-dimensional models, the tear direction should be determined by maximising $G - G_c$, where G_c is a direction-dependent material parameter. For instance, Ferrara and Pandolfi used a directional resistance surface [13, 14] to reflect the anisotropic response in the soft tissue in their cohesive-zone approach. Ultimately, models like this can be developed to study patient-specific geometries constructed from medical images and provide evidence for the potential development of arterial dissections.

5 Conclusion

We have developed computational models for predicting tear propagation in two-dimensional artery models. These models extend the Griffith energy balance principle in linear elasticity to fibre-reinforced materials with finite deformation and are verified using analytical solutions for simpler cases. The results show that the presence of fibres will in general slow down the ERR with respect to driving tear propagation due to an existing tear and that fibres aligned parallel to a tear will decrease the ERR most. However, the existence of fibres alone cannot stop the growth of tears in our models. Tear arrest occurs only when surrounding connective tissues with sufficient stiffness are included. Although the models are simplified, our work provides important insights into the behaviour of tear propagation in soft tissues.

Acknowledgments LW is supported by a China Scholarship Council Studentship and the Fee Waiver Programme at the University of Glasgow.

Appendix 1: Derivative of Cauchy stress and tangential moduli for a quasi-incompressible material (6)

Cauchy stress

Follow the standard formulas of the theory of finite elasticity, e.g. see [25]. We firstly calculate the second Piola–Kirchhoff stress,

$$\mathbf{S} = 2 \frac{\partial \Psi}{\partial \mathbf{C}} = 2 \left(\frac{\partial \Psi_v}{\partial \mathbf{C}} + \frac{\partial \Psi_m}{\partial \mathbf{C}} + \frac{\partial \Psi_f}{\partial \mathbf{C}} \right), \tag{10}$$

where

$$\begin{aligned} \frac{\partial \Psi_v}{\partial \mathbf{C}} &= \Psi'_v(J) \frac{\partial J}{\partial \mathbf{C}} = \frac{1}{2} \Psi'_v(J) J \mathbf{C}^{-1} = \frac{K}{2} (J - 1) J \mathbf{C}^{-1}, \\ \frac{\partial \Psi_m}{\partial \mathbf{C}} &= \frac{c}{2} \frac{\partial \bar{I}_1}{\partial \mathbf{C}} = \frac{c}{2} \left(J^{-2/3} \mathbf{1} - \frac{1}{3} \bar{I}_1 \mathbf{C}^{-1} \right), \\ \frac{\partial \Psi_f}{\partial \mathbf{C}} &= \sum_{n=4,6} \psi'(\bar{I}_n) \frac{\partial \bar{I}_n}{\partial \mathbf{C}} = \sum_{n=4,6} k_1 (\bar{I}_n - 1) \exp \left(k_2 [\bar{I}_n - 1]^2 \right) \left(J^{-2/3} \mathbf{M}_n - \frac{1}{3} \bar{I}_n \mathbf{C}^{-1} \right). \end{aligned} \tag{11}$$

Substitute these into (10) to obtain the explicit expression for the second Piola–Kirchhoff stress. Pushing it forward using

$$\boldsymbol{\sigma} = J^{-1} \mathbf{F} \mathbf{S} \mathbf{F}^T$$

immediately gives the Cauchy stress

$$\boldsymbol{\sigma} = K(J - 1)\mathbf{I} + \frac{c}{J} \left(\bar{\mathbf{b}} - \frac{1}{3} \bar{I}_1 \mathbf{I} \right) + \frac{2}{J} \sum_{n=4,6} k_n (\bar{I}_n - 1) \exp \left(k_2 [\bar{I}_n - 1]^2 \right) \left(J^{-2/3} \mathbf{m}_n - \frac{1}{3} \bar{I}_n \mathbf{I} \right), \tag{12}$$

where $\bar{\mathbf{b}} = J^{-2/3} \mathbf{F} \mathbf{F}^T$ and $\mathbf{m}_n = \mathbf{F} \mathbf{M}_n \mathbf{F}^T$. In particular,

$$\mathbf{m}_4 = \mathbf{a}_1 \otimes \mathbf{a}_1 \quad \text{and} \quad \mathbf{m}_6 = \mathbf{a}_2 \otimes \mathbf{a}_2,$$

where $\mathbf{a}_i = \mathbf{F} \mathbf{A}_i$ ($i = 1, 2$) represents the deformed vector of the unit vector \mathbf{A}_i characterising the orientation of the i th family of fibres in the reference configuration.

Tangent moduli

Similarly, the material tangent moduli associated with the increment of the second Piola–Kirchhoff stress \mathbf{S} and the Green strain tensor $\mathbf{E} = \frac{1}{2}(\mathbf{C} - \mathbf{I})$ is derived first:

$$\mathfrak{C} = 2 \frac{\partial \mathbf{S}}{\partial \mathbf{C}} = 2 \left(\frac{\partial \mathbf{S}^v}{\partial \mathbf{C}} + \frac{\partial \mathbf{S}^m}{\partial \mathbf{C}} + \frac{\partial \mathbf{S}^f}{\partial \mathbf{C}} \right), \tag{13}$$

where $\mathbf{S}^x = 2\partial\psi_x/\partial\mathbf{C}$, $x = \{v, m, f\}$. In index notation,

$$\begin{aligned} \frac{\partial S_{IJ}^v}{\partial C_{KL}} &= J C_{IJ}^{-1} \psi_v''(J) \frac{\partial J}{\partial C_{KL}} + \psi_v'(J) C_{IJ}^{-1} \frac{\partial J}{\partial C_{KL}} + \psi_v'(J) J \frac{\partial C_{IJ}^{-1}}{\partial C_{KL}} \\ &= \frac{1}{2} J C_{IJ}^{-1} C_{KL}^{-1} \left[(J \psi_v''(J) + \psi_v'(J)) + J \psi_v'(J) \frac{\partial C_{IJ}^{-1}}{\partial C_{KL}} \right], \\ \frac{\partial S_{IJ}^m}{\partial C_{KL}} &= c \left[-\frac{1}{3} \left(\frac{\partial \bar{I}_1}{\partial C_{KL}} C_{IJ}^{-1} + \bar{I}_1 \frac{\partial C_{IJ}^{-1}}{\partial C_{KL}} \right) + \frac{\partial J^{-2/3}}{\partial C_{KL}} \delta_{IJ} \right], \\ \frac{\partial S_{IJ}^f}{\partial C_{KL}} &= \sum_{n=4,6} 2 \left[\psi''(\bar{I}_n) \frac{\partial \bar{I}_n}{\partial C_{IJ}} \frac{\partial \bar{I}_n}{\partial C_{KL}} - \frac{1}{3} \psi'(\bar{I}_n) \left(\frac{\partial \bar{I}_n}{\partial C_{KL}} C_{IJ}^{-1} + \bar{I}_n \frac{\partial C_{IJ}^{-1}}{\partial C_{KL}} + J^{-2/3} C_{KL}^{-1} A_{IJ} \right) \right]. \end{aligned} \tag{14}$$

We note some useful differentials:

$$\begin{aligned} \frac{\partial C_{IJ}^{-1}}{\partial C_{KL}} &= -\frac{1}{2} \left(C_{IK}^{-1} C_{JL}^{-1} + C_{IL}^{-1} C_{JK}^{-1} \right), \\ \frac{\partial \bar{I}_1}{\partial C_{IJ}} &= -\frac{1}{3} \bar{I}_1 C_{IJ}^{-1} + J^{-2/3} \delta_{IJ}, \quad \psi_v'(J) = K(J - 1), \quad \psi_v''(J) = K, \\ \frac{\partial \bar{I}_n}{\partial C_{IJ}} &= -\frac{1}{3} \bar{I}_n C_{IJ}^{-1} + J^{-2/3} A_{IJ}, \quad n = 4, 6, \end{aligned}$$

$$\begin{aligned} \psi'(\bar{I}_n) &= k_1(\bar{I}_n - 1) \exp\left(k_2[\bar{I}_n - 1]^2\right), \\ \psi''(\bar{I}_n) &= k_1 \exp\left(k_2[\bar{I}_n - 1]^2\right) \left[1 + 2k_2(\bar{I}_n - 1)^2\right]. \end{aligned}$$

Substituting (14) into (13) gives the explicit expression for the material tangent moduli. Pushing it forward gives the spatial tangent moduli required by a user-provided material model in FEAP. Its components are as follows:

$$\begin{aligned} c_{ijkl} &= \frac{1}{J} F_{iI} F_{jJ} F_{kK} F_{lL} \mathfrak{C}_{IJKL} \\ &= \delta_{ij} \delta_{kl} \left[J \Psi''_v(J) + \Psi'_v(J) \right] - \Psi'_v(J) (\delta_{ik} \delta_{jl} + \delta_{il} \delta_{jk}) \\ &\quad - \frac{2}{3} \frac{c}{J} \left[-\frac{1}{3} \bar{I}_1 \delta_{kl} \delta_{ij} + \delta_{ij} \bar{b}_{kl} + \delta_{kl} \bar{b}_{ij} - \frac{\bar{I}_1}{2} (\delta_{ik} \delta_{jl} + \delta_{il} \delta_{jk}) \right] \\ &\quad + \frac{4}{J} \sum_{n=4,6} \left\{ \psi''(\bar{I}_n) \left(-\frac{1}{3} \bar{I}_n \delta_{ij} + J^{-2/3} m_{nij} \right) \left(-\frac{1}{3} \bar{I}_n \delta_{kl} + J^{-2/3} m_{nkl} \right) \right. \\ &\quad \left. - \frac{1}{3} \psi'(\bar{I}_n) \left[-\frac{1}{3} \bar{I}_n \delta_{ij} \delta_{kl} - \frac{\bar{I}_n}{2} (\delta_{ik} \delta_{jl} + \delta_{il} \delta_{jk}) + J^{-2/3} (m_{nij} \delta_{kl} + \delta_{ij} m_{nkl}) \right] \right\}. \end{aligned} \tag{15}$$

Finally, transforming (12) and (15) into the corresponding matrix form gives all formulas for the user subroutine for the HGO material model.

Appendix 2: Verification of material model for simple cases

We verify our model on the basis of comparisons with analytical results for a plane strain problem for a unit-square sample of fibre-reinforced material. For simplicity, both families of fibres have the same orientation, along the x -axis.

Firstly, we stretch the block along the x -axis with a stretch ratio λ_x . Plane strain and incompressibility ensure that the deformation gradient can be written as

$$\mathbf{F} = \begin{pmatrix} \lambda_x & 0 & 0 \\ 0 & 1/\lambda_x & 0 \\ 0 & 0 & 1 \end{pmatrix}. \tag{16}$$

Substituting (16) into (4) gives the corresponding strain energy (Fig. 14). For an incompressible material (4) we derive the Cauchy stress

$$\boldsymbol{\sigma} = -\mathfrak{L} \mathbf{1} + c \mathbf{b} + \sum_{n=4,6} 2\psi'(I_n) \mathbf{m}_n, \tag{17}$$

where \mathfrak{L} is the Lagrange multiplier. Without loss of generality, we consider a material with both families of fibres along the horizontal direction, $\mathbf{A}_1 = \mathbf{A}_2 = [1, 0, 0]^T$. Substituting (16) into (17) gives the Cauchy stress

$$\boldsymbol{\sigma} = -\mathfrak{L} \mathbf{1} + c \begin{pmatrix} \lambda_x^2 & 0 & 0 \\ 0 & 1/\lambda_x^2 & 0 \\ 0 & 0 & 1 \end{pmatrix} + 2\psi'(I_4) \begin{pmatrix} \lambda_x^2 & 0 & 0 \\ 0 & 0 & 0 \\ 0 & 0 & 0 \end{pmatrix}. \tag{18}$$

Since the surfaces with normal directions parallel to the y -axis are traction free, we have

$$0 = \sigma_{yy} = -\mathfrak{L} + 1/\lambda_x^2, \tag{19}$$

and thus $\mathfrak{L} = 1/\lambda_x^2$. Substituting into (18) we have

$$\sigma_{xx} = -1/\lambda_x^2 + c\lambda_x^2 + 2\psi'(\lambda_x^2)\lambda_x^2. \tag{20}$$

This analytical response is shown in Fig. 15.

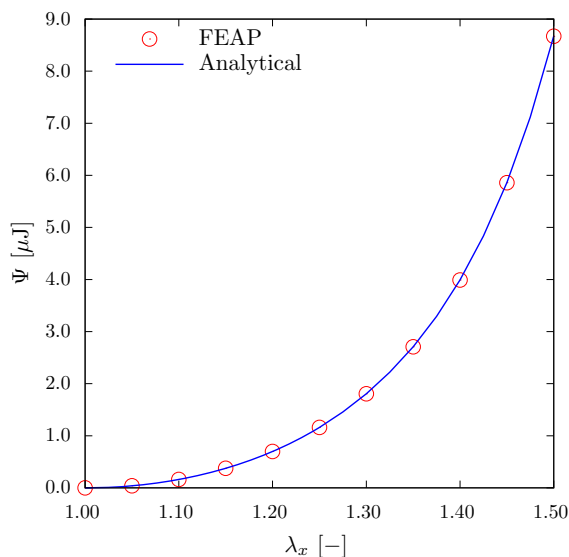


Fig. 14 The stored energy calculated by the computational model agrees with the analytical expression for the energy in a simple tension experiment

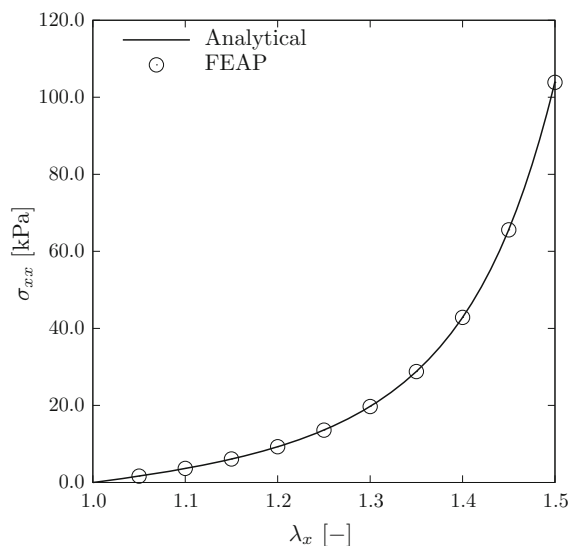


Fig. 15 Verification of model for HGO material against analytical results for principal longitudinal stress σ_{xx} vs. stretch λ_x

We now compare the analytical with the numerical results. In the computations, the penalty parameter K in (6) is chosen to be 10^5 , at which value or greater the numerical results agree with analytical predictions for both the energy (Fig. 14) and stress (Fig. 15).

Appendix 3: A simple beam model for ERR

Inequality (2) is known as the Griffith criterion when applied to linear elastic problems. Consider a beam of constant Young's modulus E and second moment of area J . The beam is bonded to a surface except for a region $0 \leq x \leq a$, where x measures the length along the beam from one end. The deflection of the beam is $w(x)$, and the boundary conditions are

$$w(x) = 0 \quad \text{for } x \geq a, \quad w''(0) = 0, \quad w'''(0) = 0. \quad (21)$$

The equation satisfied by $w(x)$ depends on the loading experienced by the beam. We take a general function $F(x, w)$ so that

$$EJw''''(x) = F(x, w). \quad (22)$$

Different choices of $F(x, w)$ give different external boundary conditions, e.g. in what follows we simulate the effect of the constraint of the surrounding connective tissue. In particular, we are interested in the calculation of the mechanical energy

$$\Pi(a) = \frac{1}{2} \int_0^\infty EJ (w''(x))^2 dx + \int_0^\infty f(x, w) dx, \quad (23)$$

where $F(x, w) = -\partial f / \partial w$ and $G = -d\Pi / da$. For a given value of G_c , (23) enables us to use (2) to determine whether a tear of length a can propagate.

We now use this simple beam model to explore the type of phenomena we obtained from the numerical experiments. To simulate the boundary condition, we set $F(x, w) = p$, a constant. Solving the ordinary differential beam equation (22) gives

$$w(x) = \begin{cases} \frac{p}{24EJ} (x^4 - 4a^3x + 3a^4) & x < a, \\ 0 & x > a, \end{cases} \quad (24)$$

and therefore, substituting into (23), we find that

$$\Pi(a) = -\frac{p^2 a^5}{40EJ}. \quad (25)$$

The energy release rate is

$$G = -\frac{d\Pi}{da} = \frac{p^2 a^4}{8EJ}. \quad (26)$$

G is a monotonically increasing function of a and p , and therefore an increase in either the length of the unbonded region (the tear) or the pressure results in the propagation of the tear being energetically favourable.

To consider the effect of surrounding connective tissues, we set $F(x, w) = p - kw$, where the constant k is the stiffness per unit length of the springs, as shown in Fig. 16. Consequently, $f = -pw + kw^2/2$, and the solution for $w(x)$ is

$$w(x) = \frac{p}{k} + W(x), \quad (27)$$

where $W(x)$ satisfies

$$W'''' + 4\lambda^4 W(x) = 0, \quad \lambda^4 = \frac{k}{4EJ}. \quad (28)$$

This is solved to give

$$W(x) = e^{-\lambda x} [A \cos(\lambda x) + B \sin(\lambda x)] + e^{\lambda x} [C \cos(\lambda x) + D \sin(\lambda x)], \quad (29)$$

with A , B , C and D chosen to satisfy the boundary conditions. Non-dimensionalising the deflection with p/k and x , with $(4EJ/k)^{1/4}$, leads to the canonical problem

$$\frac{d^4 y}{ds^4} = 4 - 4y, \quad (30)$$

with boundary conditions $y''(0) = y'''(0) = 0$ and $y(\alpha) = y'(\alpha) = 0$, where $\alpha = a/l$. The solution to this problem is

$$y(s) = 1 + \frac{(\sin s \cosh s + \cos s \sinh s) (\cos \alpha \sinh \alpha - \sin \alpha \cosh \alpha) - 2 \cos s \cosh s \cos \alpha \cosh \alpha}{\cos^2 \alpha + \cosh^2 \alpha}. \quad (31)$$

The mechanical energy is

$$\Pi = \left(\frac{p}{k}\right)^2 EJ \frac{l}{l^4} \int_0^\alpha \frac{1}{2} (y''(s))^2 ds + \frac{1}{2} k \left(\frac{p}{k}\right)^2 l \int_0^\alpha y(s)^2 ds - \frac{p^2}{k} l \int_0^\alpha y(s) ds. \quad (32)$$

This expression simplifies to

$$\Pi = \frac{p^2 l}{k} \left[\int_0^\alpha \frac{1}{8} (y''(s)^2 + 4y(s)^2) - y(s) ds \right], \quad (33)$$

and then we obtain the ERR

$$G = -\frac{d\Pi}{da} = -\frac{p^2}{k} \left\{ \frac{1}{8} [y''(\alpha)^2 + 4y(\alpha)^2] - y(\alpha) \right\}. \quad (34)$$

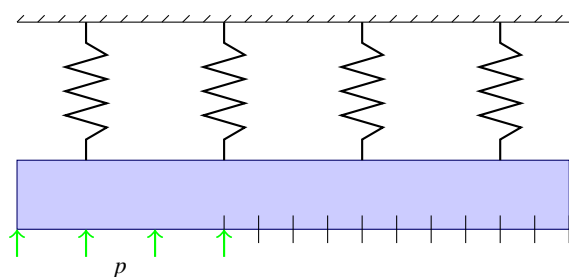


Fig. 16 Effect of connective tissue using beam model. The semi-infinite beam, of constant Young's modulus E and second moment of area J , is bonded to a surface except for a region $0 < x < a$, which represents the tear. The spring bed represents the surrounding connective tissues

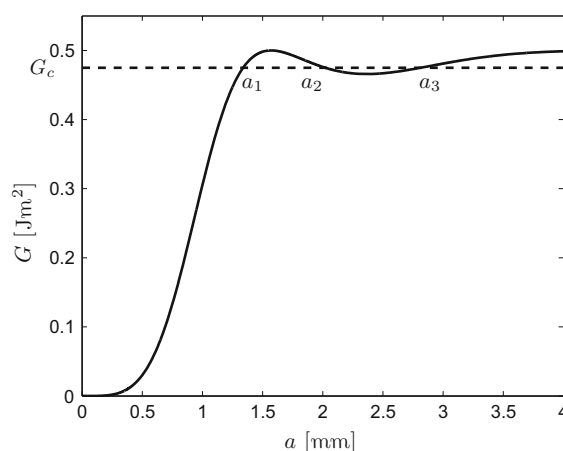


Fig. 17 Tear arrest is also demonstrated by the beam model when connective tissue is present. The ERR G is no longer a monotonic function of a , and for a given critical value G_c , a tear of length a , where $a_1 < a < a_2$ or $a > a_3$, will propagate. However, the tear arrests when $a_2 < a < a_3$

We display the curve of $G(a)$ for a set of typical parameters in Fig. 17. When subject to a constant pressure, $G(a)$ is not a monotonically increasing function of a , and propagation arrest occurs. This is qualitatively similar to what is seen in Fig. 12 in the numerical simulations for a strip of fibre-reinforced tissues subject to finite strain.

References

1. Khan IA, Nair CK (2002) Clinical, diagnostic, and management perspectives of aortic dissection. *Chest J* 122(1):311–328
2. Foundation MHI (2013) Mortality for acute aortic dissection near one percent per hour during initial onset. ScienceDaily, 10 March 2013. www.sciencedaily.com/releases/2013/03/130310164230.htm. Accessed 6 January 2015
3. Rajagopal K, Bridges C, Rajagopal K (2007) Towards an understanding of the mechanics underlying aortic dissection. *Biomech Model Mechanobiol* 6:345–359
4. de Figueiredo Borges L, Jaldin RG, Dias RR, Stolf NAG, Michel JB, Gutierrez PS (2008) Collagen is reduced and disrupted in human aneurysms and dissections of ascending aorta. *Hum Pathol* 39(3):437–443
5. Tada H, Paris PC, Irwin GR, Tada H (2000) *The stress analysis of cracks handbook*. ASME Press, New York
6. Krishnan VR, Hui CY, Long R (2008) Finite strain crack tip fields in soft incompressible elastic solids. *Langmuir* 24(24):14245–14253
7. Stephenson RA (1982) The equilibrium field near the tip of a crack for finite plane strain of incompressible elastic materials. *J Elast* 12(1):65–99
8. Ionescu I, Guilkey JE, Berzins M, Kirby RM, Weiss JA (2006) Simulation of soft tissue failure using the material point method. *J Biomech Eng* 128(6):917
9. Volokh KY (2004) Comparison between cohesive zone models. *Commun Numer Methods Eng* 20(11):845–856
10. Gasser TC, Holzapfel GA (2006) Modeling the propagation of arterial dissection. *Eur J Mech A* 25(4):617–633
11. Elices M, Guinea G, Gomez J, Planas J (2002) The cohesive zone model: advantages, limitations and challenges. *Eng Fract Mech* 69(2):137–163
12. Bhattacharjee T, Barlingay M, Tasneem H, Roan E, Vemaganti K (2013) Cohesive zone modeling of mode I tearing in thin soft materials. *J Mech Behav Biomed Mater* 28:37–46
13. Ferrara A, Pandolfi A (2008) Numerical modelling of fracture in human arteries. *Comput Methods Biomech Biomed Eng* 11(5):553–567
14. Ferrara A, Pandolfi A (2010) A numerical study of arterial media dissection processes. *Int J Fract* 166(1–2):21–33
15. Ortiz M, Pandolfi A (1999) Finite-deformation irreversible cohesive elements for three-dimensional crack-propagation analysis. *Int J Numer Methods Eng* 44(9):1267–1282
16. Griffith AA (1921) The phenomena of rupture and flow in solids. *Philos Transa R Soc Lond Ser A* 221:163–198

17. Irwin G, Wells A (1965) A continuum-mechanics view of crack propagation. *Metallurg Rev* 10(1):223–270
18. Willis J (1967) A comparison of the fracture criteria of Griffith and Barenblatt. *J Mech Phys Solids* 15(3):151–162
19. Zehnder AT (2012) Fracture mechanics. Lecture notes in applied and computational mechanics, vol 62. Springer
20. Knees D, Mielke A (2008) Energy release rate for cracks in finite-strain elasticity. *Math Methods Appl Sci* 31(5):501–528
21. Taylor RL (2011) FEAP—a finite element analysis program: Version 8.3 User manual. University of California at Berkeley
22. Holzapfel GA, Gasser TC, Ogden RW (2000) A new constitutive framework for arterial wall mechanics and a comparative study of material models. *J Elast* 61(1):1–48
23. Flory P (1961) Thermodynamic relations for high elastic materials. *Trans Faraday Soc* 57:829–838
24. Taylor RL (2011) FEAP—a finite element analysis program: Version 8.3 Programmer manual. University of California at Berkeley
25. Holzapfel GA (2000) Nonlinear solid mechanics: a continuum approach for engineering. Wiley, New York